

# Accurate Measurement Method for Tube's Endpoints Based on Machine Vision

LIU Shaoli, JIN Peng, LIU Jianhua\*, WANG Xiao, and SUN Peng

*School of Mechanical Engineering, Beijing Institute of Technology, Beijing 100081, China*

Received November 11, 2015; revised May 9, 2016; accepted May 16, 2016

**Abstract:** Tubes are used widely in aerospace vehicles, and their accurate assembly can directly affect the assembling reliability and the quality of products. It is important to measure the processed tube's endpoints and then fix any geometric errors correspondingly. However, the traditional tube inspection method is time-consuming and complex operations. Therefore, a new measurement method for a tube's endpoints based on machine vision is proposed. First, reflected light on tube's surface can be removed by using photometric linearization. Then, based on the optimization model for the tube's endpoint measurements and the principle of stereo matching, the global coordinates and the relative distance of the tube's endpoint are obtained. To confirm the feasibility, 11 tubes are processed to remove the reflected light and then the endpoint's positions of tubes are measured. The experiment results show that the measurement repeatability accuracy is 0.167 mm, and the absolute accuracy is 0.328 mm. The measurement takes less than 1 min. The proposed method based on machine vision can measure the tube's endpoints without any surface treatment or any tools and can realize on line measurement.

**Keywords:** machine vision, non-contact measurement, reflection light, tube endpoint measurement

## 1 Introduction

Tube system is used widely in aviation, aerospace, shipbuilding, and automotive industries. It is responsible for transmission of gases and liquids, and forms an important part of many mechanical and electrical products. The tube is the major component of a tube system. The process precision of tube has an important impact on assembling reliability and products performance<sup>[1]</sup>.

A tube is usually formed using a computer numerical control(CNC) tube bending machine. In the processing, a certain degree of resilience will be produced, which will lead to a certain bias between the tube product and the design model. To ensure springback compensation<sup>[2]</sup> in the process, which will help to achieve stress-free assembly, the accurate measurement and reconstruction of a tube's three-dimensional(3D) geometrical shape is important.

In particular, because a tube's endpoints have to assemble with other devices, the manufacturing accuracy of the tube endpoints must be controlled strictly. Thus, the accurate measurement of a tube's endpoint and the corresponding correction of the geometric errors is an important matter. According to the investigation, the measurement accuracy of tubes' endpoints should be less than about 0.5 mm.

Traditional measurement methods for a tube's endpoints include the coordinate measuring machine(CMM) method, a handheld mechanical arm, and methods based on laser scanning devices.

The measurement accuracy of a CMM is high, but the measurement environment is strict, and the measuring range is limited. Also, a large tube cannot be measured by a handheld mechanical arm. Measurement methods based on laser scanning<sup>[3-4]</sup> require workers to move the laser probe carefully along the tube. Thus, it is difficult to operate. In addition, these three methods are all time-consuming and the workers' workload is extensive.

In recent years, 3D measuring techniques based on machine vision have developed rapidly due to the following advantages: non-contact data acquisition, high precision, fast measurements, good flexibility, and a higher level of automation. Such methods<sup>[5-7]</sup> are used widely in dimension measurement of parts and free-form surface. However, for the accurate measurement of a tube's endpoint, most studies<sup>[8-11]</sup> complete the measurements by fitting elliptical or semi-elliptical of the tube's end in two-dimensional(2D) images to locate the endpoints coordinates. This method can produce good results in cases where the edge of tube's end in the 2D image has a relatively complete ellipse. For example, BERGAMASCO, et al<sup>[9]</sup>, proposed to layout cameras near the tube's end. Therefore, the edge of tube's end in the image is large and clear enough to extract the endpoints by fitting elliptical method. However, the position of the camera must be adjusted repeatedly according to the pose and length of the

\* Corresponding author. E-mail: jeffliu@bit.edu.cn

Supported by National Natural Science Foundation of China(Grant No. 51305031)

© Chinese Mechanical Engineering Society and Springer-Verlag Berlin Heidelberg 2016

tube. Also, camera calibration should be repeated for every measurement. Moreover, these cameras cannot capture the whole shape of tube. Thus, for the 3D shape measurement of the tube, additional cameras are needed.

Additionally, the common disadvantage of the fitting elliptical method is that the center of the ellipse and the true projected center of the circular object target are not identical<sup>[12]</sup>, which tends to produce positioning error. The endpoints' shapes in the 2D images differ with different camera's viewing angles and different diameters of tubes. When the diameter of the tube is small, the projection of the tube's endpoint is almost impossible to fit with an ellipse. Thus, traditional contour-fitting algorithms are less than ideal.

JIN, et al<sup>[13]</sup>, proposed a measurement method based on a 2D target, which transforms the identification of the endpoint into the identification of a target mark point. This method avoids direct extraction of the edge of the tube's end in the image; thus, it can achieve good results. However, this method requires a pair of targets corresponding to different tube diameters. Therefore, it has a higher cost.

Besides the tube's endpoints location method, the image quality is the most important factor to affect the measurement accuracy in a machine vision-based measurement. An appropriate method of lighting can improve the measurement accuracy by enhancing contrast of the tube and the background. However, due to the illumination and the circular arc surface of the tube, light is reflected from the tube's surface, which affects the stability of the image processing algorithms and, ultimately, the measurement accuracy of the tube's endpoints. Thus, reflective light processing of the tube's surface is important. The reflective light on an object's surfaces is divided into two categories: specular light and diffuse light<sup>[14]</sup>. Traditional machine-vision algorithms are based on the lambertian assumption of a diffuse surface. Thus, the existence of specular light causes partial loss of the objects' information, which may result in misextraction of an interest region or even failure. Thus, using image information to remove specular light on the surface is an important issue. Presently, the main method for removing the reflective light is to separate the specular light and diffuse light using colorimetric and polarization analyses. For example, WOLFF, et al<sup>[15]</sup>, first proposed using the different polarization characteristics between diffuse light and specular light to separate them. Based on their research, UMEYAMA, et al<sup>[16]</sup>, proposed that using light polarization analysis combined with statistical image analysis could separate the two reflective light components. Based on a chromatic reflection model<sup>[14]</sup>, SATO, et al<sup>[17]</sup>, obtained different images of the object under different illumination angles by moving the light source, and calculated the specular light on the object's surface by analyzing the color component of sequential images. KLINKER, et al<sup>[18]</sup>, proposed to separate the specular light and diffuse light by

an analysis of the main components of the two lights. NOVAK, et al<sup>[19]</sup>, estimated the geometry and roughness of the object by analyzing the distribution of the image pixels in RGB space first, from which the specular light on the surface of the object could be calculated. These methods are all based on chromaticity space and need to use the image's color information. Therefore, they are only applied to color images and cannot be used directly with gray-scale images, which contain only brightness information. As such, new methods are required for gray-scale images. CHING, et al<sup>[20]</sup>, took gray images from multiple angles. Then, maximum peak information from a histogram and correlation coefficients of best matching were then used to detect and remove the specular light. WANG, et al<sup>[21]</sup>, and JIANG, et al<sup>[22]</sup>, proposed removing specular light from a single image by equalizing the brightness information of the image. However, this method can only improve the visual effect and did not actually remove the specular light.

Based on the analysis above, we can see machine vision-based measurement methods for tubes have developed rapidly and have also been used in engineering<sup>[23]</sup>. However, questions remain regarding as follows.

#### (1) Removing the specular light on a tube's surface

Due to the presence of a light source in the measurement system, specular light on a tube's surface is almost inevitable. This condition greatly affects the accuracy of image-processing algorithms, resulting in a decline in tube measuring accuracy.

#### (2) Location method for a tube's endpoints

Presently, the main idea used to recognize and reconstruct a tube's endpoints is fitting the circle arc profiles of the tube's end. This method has a better effect when the 2D image of the tube's end is enhanced. Because the pose and diameter of the tube and the visual angle of the camera differ, the shape of the tube's end in the images is also very different, as shown in Fig. 1.

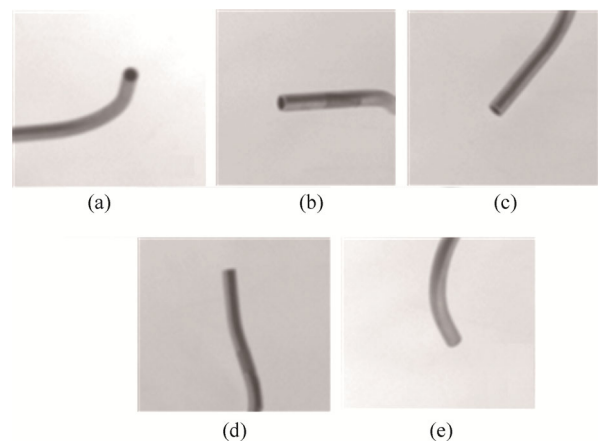


Fig. 1. Shapes of a tube's end in images

Here, we proposed a new image processing method that used photometric linearization to remove the specular light on the tube's surface and the reflected light. The edge extraction accuracy of the tube region can be improved

markedly, which is basis for subsequent location of the tube's endpoints. In particular, the method can also be used to process the images of other objects that are measured based on machine vision. In this study, we also developed an optimization model for a tube's endpoint location. Based on the proposed model and the principle of stereo matching, the global coordinates and the relative distance of the tube's endpoints can be obtained.

## 2 Illumination and Reflection Process Analysis

### 2.1 Illumination method

In a machine vision-based measurement system, the light source is an important component. A light source projects light onto the object surface to highlight the characteristics of the tube, and then, the camera captures the images from which features can be extracted. Reasonable illumination can improve image quality, reducing difficulties in image processing.

The general principles of illumination are to highlight the important features of the object to be measured in the image while suppressing unwanted features. In multi-vision-based tube measurement, the contour edges of the tube are important features for 3D reconstruction of the tube, while the texture of the tube's surface, such as nicks, is unimportant. Thus, a backlight is often selected for the system. The effect of the backlight is closely related to the thickness of the object. When the object is thinner, the sides of the object do not reflect light. Then, at the edges of the object, a strong contrast boundary can form. Thus, a backlight can extract edges of a thinner object better. When the measured object has a certain thickness, due to the diffuse characteristics of the backlight, the edges will appear to contract inward. In particular, the arc contour shape of a tube and the metal material characteristics contribute to a large amount of reflected light along the edge, which is captured by the camera. Thus, the contrast of the tube's edge with the background can be reduced greatly, as shown in Fig. 2. Also, the reflective areas on both sides of the object are asymmetrical. When the brightness of the light source is high and the tube's surface roughness is good, the light will cause strong reflection on the tube's surface, which could seriously weaken the tube's edge or even make it difficult to see. This will significantly affect image processing of the tube.

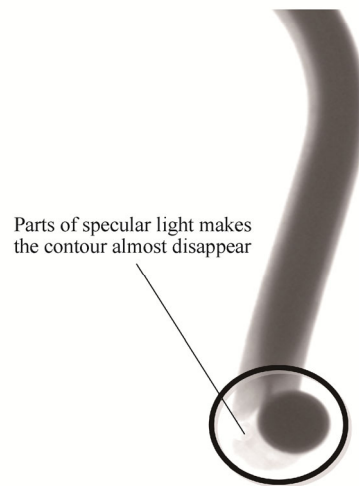
### 2.2 Reflection mechanism analysis

With backlight illumination, parts of tube's edge are illuminated almost to the same extent as the backlight, forming a clear difference with the center of the tube, as shown in Fig. 2. Based on a color reflection model<sup>[14]</sup>, the reflective light on the tube's surface is divided into specular light and diffuse light. The specular light makes the contour line of the tube disappear, which severely impacts the image processing of tubes. The existence of reflected light

seriously disturbs the effects of segmentation and edge detection, which are all based on gray values. This will result in a segmentation region and edge inward contraction, compared with the realistic edge.



(a) Edge of the tube with reflected light



(b) Specular light influence

Fig. 2. Tube with a backlight source

Given the roughness characteristics of a tube's surface, the light is more complicated in the case of the tube's reflecting surfaces. The reflecting situation is shown in Fig. 3, where the reflective component includes the following situations:

(1) When the bin size is similar to the wavelength of light, the incident light will cause diffraction and scattering at the point of incidence, and then decompose to reflected light in different directions.

(2) Because some portions of the tube's surface are rough, the light between its bin size on the surface may emit after several reflections.

(3) The incident light may be transmitted into the interior of the tube, and reflect with pigment inside the tube, then reflect into space.

(4) Light reflects once in a relatively smooth section of the tube and launches into space.

In this reflection model, reflected light (1)–(3) is referred to as diffuse reflection, while reflected light (4) is referred to as specular reflection.

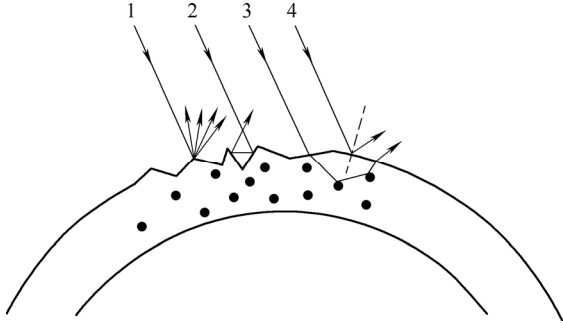


Fig. 3. Microstructure of a tube's surface and light reflections

According to the reflective component framework<sup>[24]</sup>, the reflection on the tube's surface is divided into diffuse reflection, specular lobes, and a specular reflection peak, as shown in Fig. 4. Because specular reflection peaks are only observed within a small scope, the effects can be ignored.

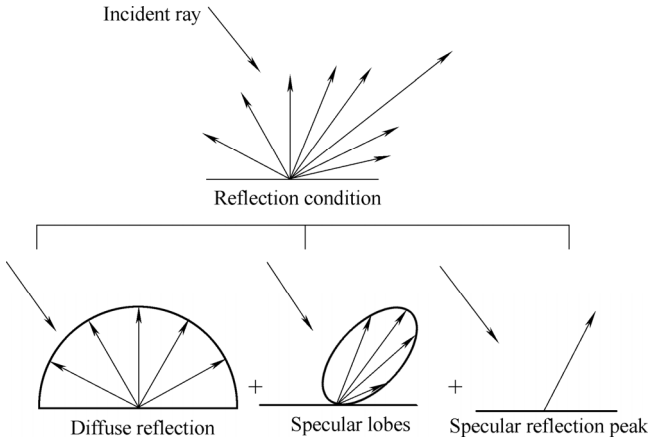


Fig. 4. Reflection components on a tube's surface

In fact, accurate segmentation is based on the characteristic of backlight illumination that it will generate strong contrast between the shadow of the object and the backlight. In an ordinary way, the shadows of objects can be divided into attachment shadows and cast shadows. Attachment shadows fall on the object, and cast shadows fall outside the object. Due to the use of a backlight, images of tubes taken by cameras only have attachment shadows of the tube, and there are no cast shadows.

### 3 Reflective Processing Algorithms

#### 3.1 Lambertian reflection model

The traditional reflective processing algorithms for images under machine vision are based on a Lambertian reflection model. The model is based on three assumptions: (1) the surfaces of the object are ideal scattering surfaces and the reflected light is diffuse; (2) the radiation source is a point light source located at infinity; and (3) the object and the camera are fixed, thus, the direction of the light changes during image capture. The intensity  $I(p)$  of a point  $p$  in the image can be expressed as

$$I(p) = \mathbf{n}_p \cdot \mathbf{s}, \quad (1)$$

where  $\mathbf{n}_p$  is the surface property vector of point  $p$ , and  $\mathbf{s}$  is the illumination properties vector. Based on Eq. (1), we know that if the angle between  $\mathbf{n}_p$  and  $\mathbf{s}$  is an obtuse angle, then,  $I(p)$  is negative, which is the area of attached shadows. This conflicts with the gray-scale scope of images. Thus, with the Lambertian reflection model, the expression of an image grayscale can be written as

$$I(p) = \max(\mathbf{n}_p \cdot \mathbf{s}, 0). \quad (2)$$

SHASHUA<sup>[25]</sup> studied the combined luminosity under a reflection model of arbitrary order. The research showed that under the reflection model with order  $k$ , the effect of changing the direction and strength of the point light source can be decomposed into linear combinations of  $k$  images of the same object. The Lambertian reflective model belongs to the third-order reflection model. Thus, any point's intensity  $I_k$  can be generated by a linear combination of three point intensities,  $I_1$ ,  $I_2$ , and  $I_3$ , in three different images(also called basic images):

$$I_k = c_k^1 I_1 + c_k^2 I_2 + c_k^3 I_3, \quad (3)$$

where  $c_k^1$ ,  $c_k^2$ ,  $c_k^3$  is the linear combination coefficient of the image. Based on the Lambertian reflection model, Eq. (3) applies to all image pixels. Thus, for an image captured under a new direction of light, the linear combination coefficients can be solved for any three pixels in the basic images. This conclusion also applies to a situation where only the illumination intensity changes, but the light direction remains fixed.

#### 3.2 Photometric linearization method

In an actual image, due to the specular light and shadow on the object's surface, Eq. (3) is not always valid. Thus, the method of photometric linearization is used to approximate Eq. (3). The basic idea of the method is selecting three images from several images under different light intensities as basic images, calculating the linear combination coefficients of the rest of the images, linearizing the basic images by the obtained linear combination coefficients, and finally obtaining an image with the specular light and shadow removed.

MUKAIGAWA, et al<sup>[26]</sup>, successfully obtained the image of an object without specular light, captured in a darkroom and illuminated by a point light source. Because the background and the shadows of images captured in a darkroom are black and the reflective area is obvious, the specular light and shadow are easy to separate. However, in a tube image, because the illumination is a backlight, the reflected light on the tube's surface is similar to the background light intensity. Thus, the processing is more difficult. In the proposed approach, we assume that the tube area in the image is segmented roughly by a dynamic

thresholding method firstly. Due to the tube's reflective surface, the segmented area is the shaded area of the tube's surface and part of the reflective area, which is contractible, compared with the real region. The region of the tube that contains the reflective area can be obtained using an area expansion algorithm. This region is then used in photometric linearization(Fig. 5).

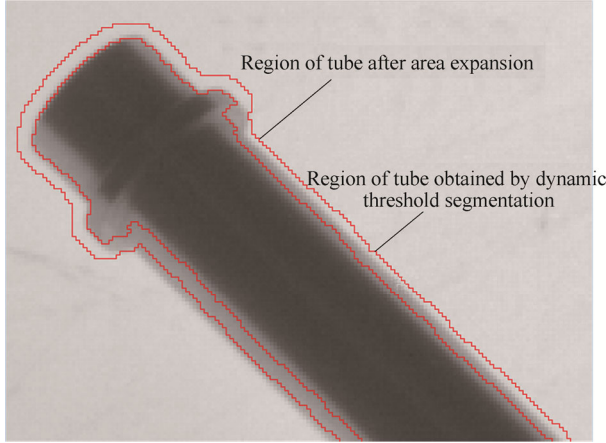


Fig. 5. Region obtained for photometric linearization

Based on the photometric linearization method,  $(I_1, I_2, \dots, I_n)$  are  $n$  images of the tube under different directions and intensities of illumination. As shown in Fig. 6,  $n=20$ , and  $(I_1, I_2, I_3)$  are three of the  $n$  images whose intensities of illumination have a large span; these three images are set as the basic images. For other images  $I_k$ , any three pixels are selected randomly in the tube's region. Eq. (3) is then used to calculate the linear combination coefficients  $c_k$  of the image.

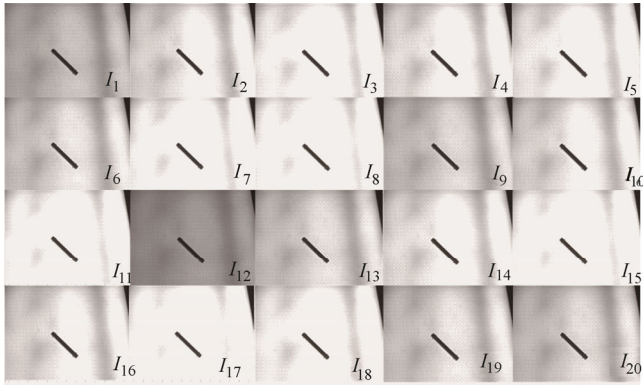


Fig. 6. Images of a tube under different illumination intensities

Based on the Lambertian model, we know that if all the images contain only diffuse light, then for any image, choosing any three pixels in the image, Eq. (4) can be used to solve the linear combination coefficients, and the result is unique.

$$\begin{pmatrix} I_k(i) \\ I_k(j) \\ I_k(m) \end{pmatrix} = \begin{pmatrix} I_1(i) & I_2(i) & I_3(i) \\ I_1(j) & I_2(j) & I_3(j) \\ I_1(m) & I_2(m) & I_3(m) \end{pmatrix} \begin{pmatrix} c_k^1 \\ c_k^2 \\ c_k^3 \end{pmatrix}, \quad (4)$$

where  $I_k (k=4,5,\dots,n)$  are the rest of the images, with the exception of the basic images,  $i, j, m$  are any three pixels randomly selected from the tube's region in the image, and  $I_k(i), I_k(j), I_k(m)$  are the corresponding pixel values.

However, due to the presence of specular light reflection and shadow, the randomly selected pixels do not always satisfy Eq. (4), resulting in the calculation of erroneous linear combination coefficients. In this paper, we proposed repeated random sampling to solve this problem. That is, three pixels in the tube's region are selected repeatedly to calculate the linear combination coefficients, based on Eq. (4), and structure the spatial distribution schematic diagram (Fig. 7). In Fig. 7, solid circle indicates coefficient for pixels only have diffuse component and hollow circle indicates coefficient for pixels have specular reflection and shadow. If the pixels for calculation only contain diffuse reflection, then the linear combination coefficients distribute relatively densely in space; if the pixels contain both specular light and shadows, the linear combination coefficients calculated with Eq. (4) may deviate from the 'right' values. Thus, the random sampling method is used to calculate sufficient coefficients (followed by removal of the points that have a large deviation) and the center of gravity of the remaining points. The linear combination coefficient calculated by this method is more reliable.

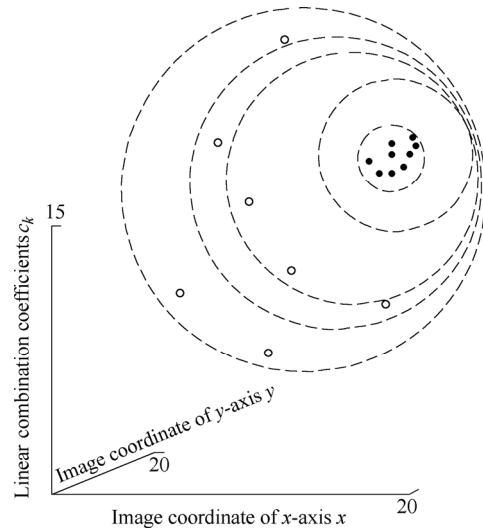


Fig. 7. Calculate result of linear combination coefficients

Fig. 8 shows a linear combination coefficients distribution of a non-basic image processed by the random sampling method and an abnormal value elimination method. It can be seen that after the processing, the coefficients were distributed over a relatively small range. Thus, the center of gravity of the coefficients can be the linear combination coefficients of the image.

After obtaining reliable linear combination coefficients of each non-basic image, selecting three images, combining the corresponding coefficient, and using Eq. (4) for reverse derivation. The brightness of the basic images  $I_1, I_2, I_3$



can be solved, and new basic images generated. This process is called base image linearization. Thus, the values of pixel intensity in the new structural image can be calculated by linear combination computing of any three non-basic images. By repeating the selection and calculation, the intensity distribution of each pixel can be generated. Similarly, the most reliable intensity of a pixel can be estimated using random sampling and an outlier elimination method. Fig. 9 shows the tube image of the third basic image in Fig. 6 after photometric linearization processing. As can be seen, after processing, the reflective region and the light source luminance value around the tube in the image have declined, compared with the original image. However, because the presence of diffuse reflection will increase the luminance of the tube's surface area, the pixel gray difference between the reflective region and shaded area is still obvious. Additionally, an obvious boundary, approximately three pixels wide, exists between the tube and the light source. Based on the boundary, the diffuse reflection area on the tube's surface can be located readily.

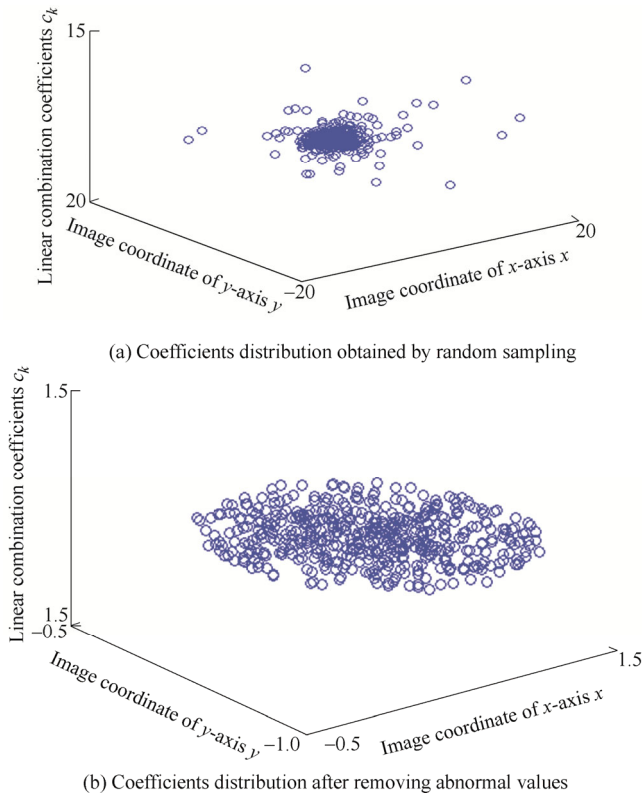


Fig. 8. Linear combination coefficients processed by random sampling and an outlier elimination method

### 3.3 Diffuse reflection area processing

After photometric linearization processing, an image of the tube containing only diffuse reflection light is obtained. However, the brightness value of the diffuse reflection component is still high and has an obvious boundary between the shaded areas. Therefore, further processing is required. The gray information in the shaded area is used to complete the complementary processing for diffuse

reflection areas. First, a circular structure of a specific radius is used to corrode the tube area, which has been divided by the dynamic threshold segmentation method. From this, the tube area only containing shadow is obtained. To effectively extract the shadow area of the tube, an interactive approach is adopted. By setting the radius of the structural elements, the corrosion range can be adjusted. Thus, the corrosion operation can be controlled dynamically.

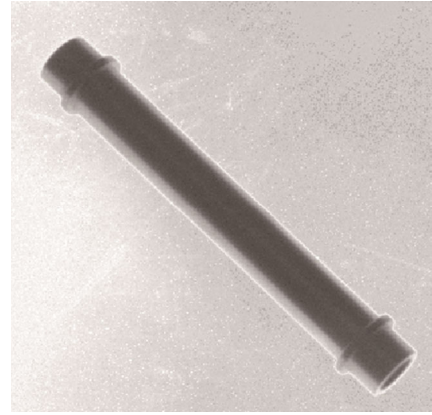


Fig. 9. Tube image after photometric linearization

Fig. 10(a) shows a partial contour of the tube's shadow area processed by the corrosion operation. Based on the shadow area, the gray histogram is calculated to determine the mode of the shaded area (Fig. 10(b)). The mode, the peak of the gray histogram, indicates that the number of pixels having this gray value in the shadow area is the largest. Using the mode to replace the gray value of other pixels in the diffuse reflection area will transform the diffuse reflection component into a shadow component. This process will eliminate the diffuse reflection area and restore the tube's region (Fig. 10(c)).

## 4 Tube Endpoint Location Algorithm

In tube assembly applications, to ensure the precise installation of tubes, accurate measurements of a tube's endpoints after the tube's bend forming are required for stress-free assembly. Previous studies mostly used the contour line fitting method to locate endpoint coordinates in each 2D image firstly. And then, a pair of images are rectified<sup>[24]</sup> which can be viewed as the process of transforming the epipolar geometry of the images into a canonical form. Finally, according to the endpoints extracted from the pair of images, the 3D coordinates can be calculated by stereo matching algorithm. However, the results of endpoints extracting vary, depending on the various shapes of the 2D projection of the tubes' endpoints, due to the different camera angles involved. Also, the projected image plane of an object circle is as an ellipse if the object plane and the image plane are not parallel to each other. However, the center of the ellipse and the true projected center of the circular object target are not

identical. Thus, the endpoints extracted from a pair images used to stereo matching may be not same point that will seriously affect the accuracy. Thus, this method is neither precise nor universal. As shown in Fig. 11, the images were the same tube which was captured by different view angles. After the image rectification and ellipse fitting, the pixel row-coordinates of endpoint  $o_1$  extracted from the left image is 791.01 and the pixel row-coordinates of endpoint  $o'_1$  extracted from the right image is 795.21. The error between the two matching points is 4 pixels which will cause mismatch and affect the measurement accuracy. Therefore, the accurate measurement of the tube's endpoints is still based on CMM or laser scanning devices. However, to improve the measurement efficiency and reduce the workload of workers, a new tube endpoint location method based on machine-vision is proposed.

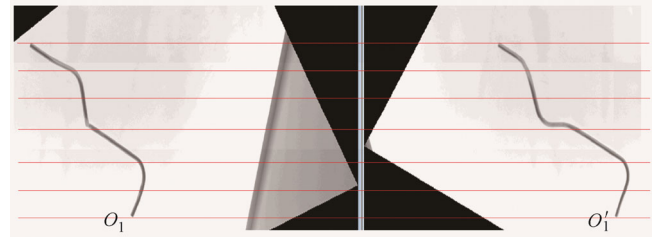


Fig. 11. Pair of tube images after rectification.

For the problems of position measurement of tube endpoints, combined with the morphological characteristics of tubes, this paper proposes a position measurement for the tube's endpoints based on the tube's centerline. This method offers the advantages of speed and versatility. Based on the processed images, from which the specular light has been removed, and by reconstruction of the centerline of the tubes, the positions of the tube's endpoints can be located using the proposed method.

The tubes studied in this paper were bent by a CNC machine. Thus, the tube's shape is subject to several specifications. The tube can be viewed as a combination of line segments and arc segments. Also, the diameter along the tube length is the same. Thus, the tube's 3D shape can be expressed by the 3D centerline and the outside diameter of the tube. The centerline can also be seen as a combination of line segments and arc segments (Fig. 12). Thus, the tube's 3D shape measurement can be converted to measurements of the diameter and the centerline of the tube. According to the technological process, the end surface of the tube will be vertical with respect to the end of the centerline upon completion. Thus, the measurement of the tube's endpoints can be converted to measurements of the intersection point of the centerline and the end surface of the tube.

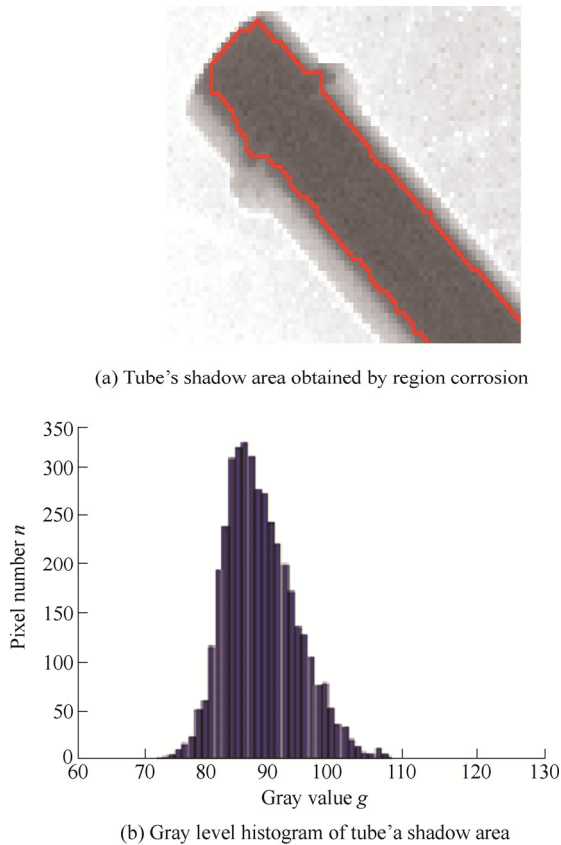


Fig. 10. Sketch map of diffuse reflection processing

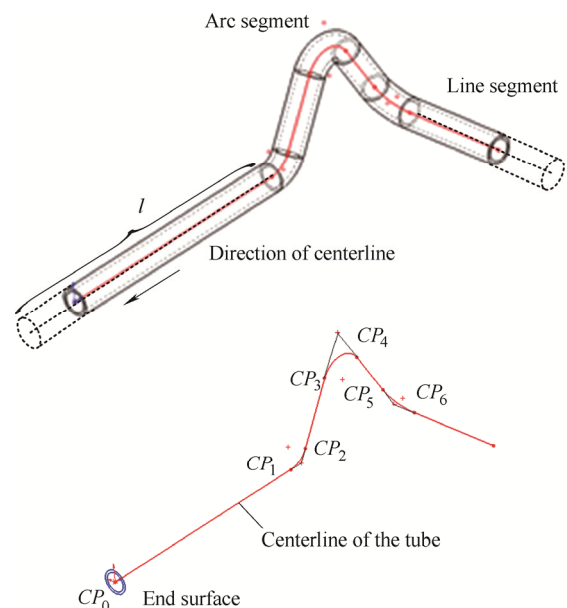


Fig. 12. Description of the tube's 3D shape

Assuming there is a cylinder at the end of the 3D model of the tube whose centerline is coincident with the centerline of the tube, the diameter of the cylinder is similar to the tube. One end's center point of the cylinder is coincident with the point of tangency of the end line and arc. As shown in Fig. 13, one end's center of the cylinder begins at  $CP_1$ . The positions of  $CP_1$  and  $CP_6$  can be calculated based on the centerline and the bending radius of the CNC machine. The length  $l$  of the cylinder is unknown and is the optimization object. Once  $l$  is obtained, the endpoints of the tube can be obtained as well. From this, the model can be optimized, as follows. We first project the 3D cylinder onto the 2D images captured by the cameras. Then, setting  $l$  as the variable and using the points on the edge of the 2D tube image (which has sub-pixel precision), the corresponding points on the edge of the projective cylinder image can be used to optimize the variable  $l$ .

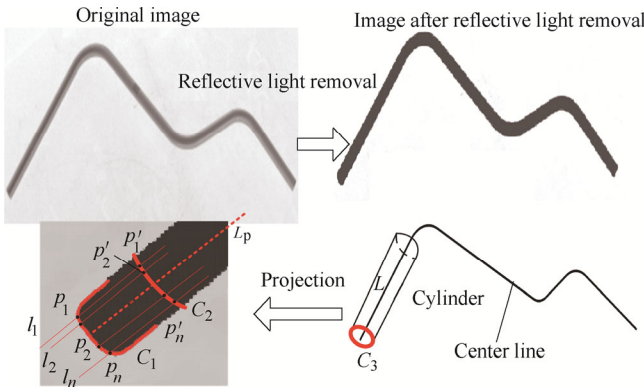


Fig. 13. Optimization model of the endpoint measurement

Fig. 12 shows that the end surface edge of the cylinder  $C_3$  is a space ellipse. Based on Eqs. (5) and (6),  $C_3$  can be projected onto the 2D image. The arc  $C_2$  is the projective edge of  $C_3$ . Similarly, the centerline  $L$  also can be projected onto the 2D image.

$$\begin{pmatrix} X_c \\ Y_c \\ Z_c \\ 1 \end{pmatrix} = \mathbf{M} \begin{pmatrix} X_w \\ Y_w \\ Z_w \\ 1 \end{pmatrix} = \begin{pmatrix} \mathbf{R} & \mathbf{T} \\ 0 & 1 \end{pmatrix} \begin{pmatrix} X_w \\ Y_w \\ Z_w \\ 1 \end{pmatrix}, \quad (5)$$

where  $\mathbf{R}$ ,  $\mathbf{T}$  is the translation relation of the camera coordinate system and the world coordinate system, which is calibrated first.  $X_w$ ,  $Y_w$ ,  $Z_w$  are the coordinate value in the world coordinate system;  $X_c$ ,  $Y_c$ ,  $Z_c$  are the coordinate value in the camera coordinate system. When the coordinate value in the world coordinate system is known, the coordinate value of any point in the camera coordinate system can be calculated with Eq. (5). Then, the coordinate value of projective point in the 2D image  $u$ ,  $v$  can be calculated using Eq. (6):

$$\begin{pmatrix} u \\ v \end{pmatrix} = \frac{f}{Z_c} \begin{pmatrix} X_c \\ Y_c \end{pmatrix}, \quad (6)$$

where  $f$  is the focal length of the camera.

As shown in Fig. 13, the points  $p_1, p_2, \dots, p_n$  are the intersection points of the lines  $l_1, l_2, \dots, l_n$ , which are parallel to the centerline's projective line  $L_p$  and the edge  $C_1$ , which is the edge of the tube in the 2D image. The points  $p'_1, p'_2, \dots, p'_n$  are the corresponding intersection points of the same lines  $l_1, l_2, \dots, l_n$  and  $C_2$ . The length  $l$  can be optimized by a least-squares method based on these points.

The method proposed differs from the traditional method, which is based on the fitting edge of the tube's end and image rectification accuracy. Thus, it overcomes the difficulties that the shape and quality of the tube's end in different images from different shooting angles are not all suitable to an elliptical fit. Also, the error which is introduced by the wrong stereo matching is avoided.

## 5 Experimental Results

### 5.1 Multi-vision-based measurement system

A multi-vision-based measurement system with a computer workstation, eight cameras, a backlight source, a measurement platform, and measurement software, is shown in Fig. 14.

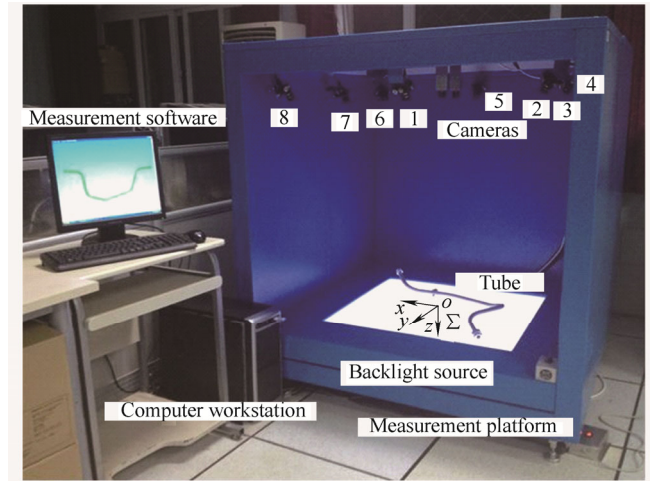


Fig. 14. Multi-vision-based measurement system

The workstation is with the Windows XP operating system, AMD Opteron 2.8GHz CPU, and 4GB RAM. The backlight source is 850×850 mm. The cameras are the monochrome CCD cameras of AVT Company in Germany, whose type are Guppy Pro F-146B. The parameters of the cameras are shown in Table 1. The general pose of the cameras can be calculated according to the range of measurement. Then the view angles of the cameras can be adjusted manually to include as the whole backlight source as possible. The accurate pose of the cameras can be



calibrated<sup>[27]</sup> in world coordinate  $\Sigma$ , where the original point  $o$  is at the center of the backlight source, the  $z$  axis of  $\Sigma$  is vertical and the  $x$  axis,  $y$  axis respectively are parallel to the margin of the backlight source. The calibration result of the cameras pose in  $\Sigma$  is shown in Table 2.

Table 2. The pose of cameras in  $\Sigma$

Camera No.	x-rotation $R_x/(^{\circ})$	y-rotation $R_y/(^{\circ})$	z-rotation $R_z/(^{\circ})$	x-translation $T_x/\text{mm}$	y-translation $T_y/\text{mm}$	z-translation $T_z/\text{mm}$
1	358.40	333.34	264.53	372.71	-15.80	-947.68
2	329.20	342.96	215.14	325.85	-501.44	-957.35
3	333.42	4.70	177.60	-161.83	-460.68	-957.40
4	336.54	27.10	134.59	-651.83	-426.81	-960.61
5	2.62	28.14	85.59	-602.41	64.58	-954.33
6	27.18	22.02	38.06	-554.10	551.37	-954.32
7	27.45	1.07	355.66	-75.10	508.64	-947.26
8	25.46	334.94	312.48	423.94	475.11	-958.23

## 5.2 Measurement experiments

### 5.2.1 Experiments regarding reflected light removal

To confirm the feasibility of the proposed reflected light removal method, 10 tubes were selected to be processed in the experiments. The diameters of the selected tubes were 6 mm, 8 mm, and 15 mm. For each tube, 20 pictures were captured by the camera with different illumination intensities but the same positions. Then, the reflected light was removed by the method described in above Section. The dynamic threshold segmentation method was used to extract the tube region of the original images and the processed images. Finally, the region extraction effects were compared.

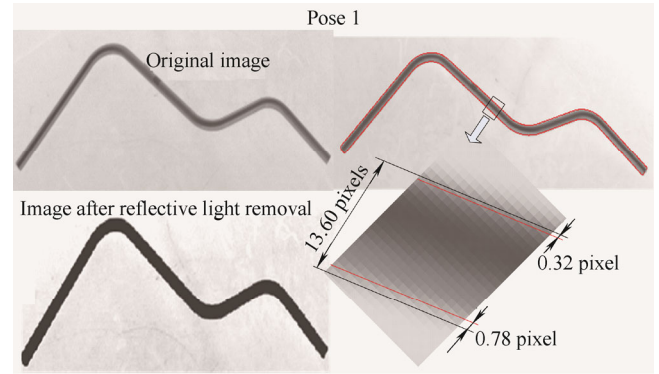
Taking one of the tubes as an example, the original image, the image after removing reflective light, and the corresponding tube region extraction images are shown in Fig. 15.

From these results, we can see that the extracted tube region of the original image is contractive, compared with the processed image. In pose 1, the tube's edge width of processed image is 13.60 pixels, while the edge extracted from original image contract inwardly 0.32 pixel and 0.78 pixel respectively, compared with the processed image. In pose 2 of the same tube, the tube's edge width of processed image is 13.58 pixels, while the edge extracted from original image contract inwardly 0.48 pixel and 0.26 pixel respectively, compared with the processed image. By system calibration, 1 pixel is 1.1mm. Then, we can know that due to the shooting angle, the contraction is more obvious on the side near the camera. The extraction results from original image of the same tube are different while the measurement position of the tube is different, which will introduce random errors. The extraction effect of the tube region based on the processed image is better, which will significantly affect the accuracy of the endpoint positions calculated. Other reflective light removal results are shown in Table 3. The edge errors between original images and

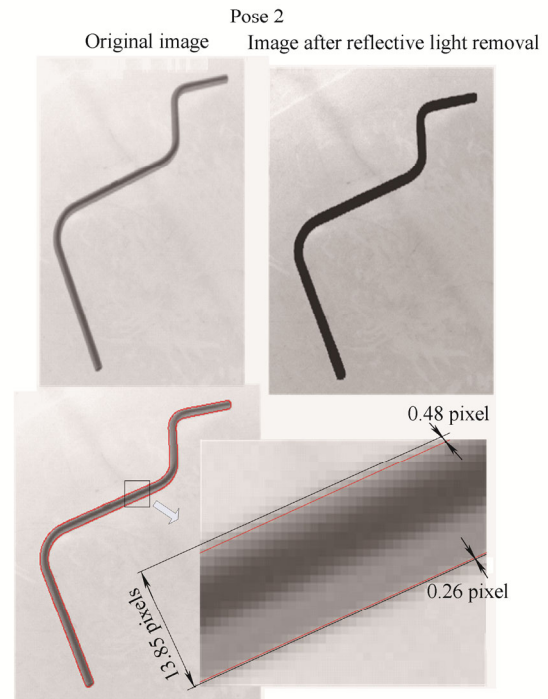
Table 1. The parameters of the cameras

Parameter	Value
Resolution $R/\text{Pixel}$	1388×1038
Frame Frequency $F/\text{fps}$	17
Camera Size $V/(\text{mm} \times \text{mm} \times \text{mm})$	48.8×29×29
Pixel Size $S/(\mu\text{m} \times \mu\text{m})$	4.65×4.65

processed images are all about 1 pixel.



(a) Edge extracting results comparison for tube in pose 1



(b) Edge extracting results comparison for tube in pose 2

Fig. 15. Comparison of the tube region extraction effects of the original and processed images

**Table 3. Reflective light removal results**

No.	Original images	Images after reflected light removal
1		
2		
3		
4		
5		
6		
7		
8		
9		
10		
11		

### 5.2.2 Experimental results of tube endpoint location

By taking 11 tubes as examples with different diameters, the distances of the endpoints of the tubes were measured by a CMM with position accuracy is 0.003 mm, from

Mitutoyo company, whose type is BLN122. We took these values as the exact values of the endpoint distances.

The measurement process of the CMM is as follows:

(1) Holding the tube on the workbench, as shown in Fig. 16;

(2) Locating the probe of CMM on the surface of the end cylinders to get about 30 points, as shown in Fig. 17. And fitting a cylinder using the points by the CMM own software;

(3) Locating the probe on the end surface of the tube to get about 10 points, as shown in Fig. 17. And fitting a plane using the points by the CMM own software;

(4) Getting the coordinate value of the tube's endpoint by the software directly, which is the intersection point of the cylinder's center line and the plane;

(5) Repeating steps (1)–(4) to get the coordinate value of the other tube's endpoint;

(6) Calculating the distance of the two endpoints.

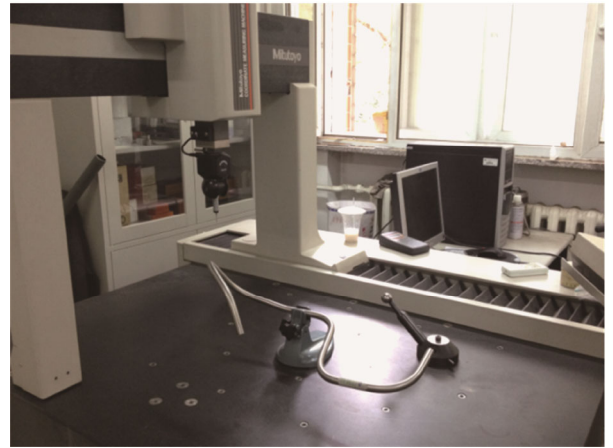


Fig. 16. Tube measurement by CMM

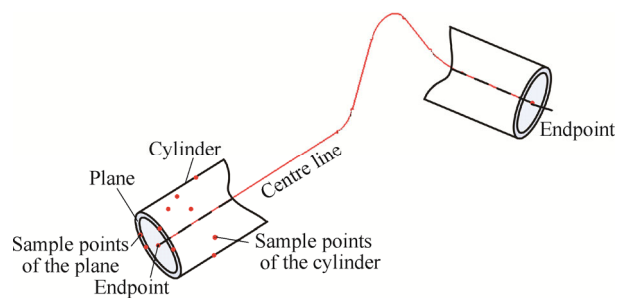


Fig. 17 Measurement of endpoints by CMM

Then, the tube was put on the backlight source of our system and transformed in 10 different positions. Based on the images where the reflective light had been removed, the endpoints of the tube were calculated by the method proposed in above Section. The results measured by CMM and our proposed method are all shown in Table 4. We calculated the average value of the results measured by our proposed method. Then, the maximum error and minimum error were also calculated by comparing every measurement result of the 10 positions to the exact value. Finally, the standard deviation of the measurement results

for every tube was calculated by

$$\sigma = \sqrt{\frac{1}{N} \sum_{q=1}^N (x_q - \mu)^2}, \quad (7)$$

where  $\sigma$  is the standard deviation,  $x_q$  is the measurement result of position  $q$ ,  $\mu$  is the average value of the measurement results of a tube,  $N$  is the measurement times.

Here, we defined the maximum standard deviation in Table 4 as the repeated accuracy of the measurement results, indicating the stability of the proposed method. Moreover,

we defined the maximum value of maximum error in Table 4 as the absolute accuracy, denoting the precision of the proposed method. Then, the absolute accuracy is 0.328 mm and the repeated accuracy is 0.167 mm. And the measurement takes less than 1 min. These results indicate that the method proposed in this paper is effective and stable. It can be used to calculate the distance between two endpoints of a tube accurately under any shooting angle. Compared with the conventional method of tube measurement, the measurement speed is rapid. The quality and shape of the tube's end 2D image does not have as much of an effect using the proposed approach.

**Table 4. Experimental results of tube endpoint location (unit: mm)**

Tube No.	1	2	3	4	5	6	7	8	9	10	11
position1 $x_1$	498.898	311.028	357.752	256.565	290.224	266.408	337.396	489.019	374.215	648.480	353.576
position2 $x_2$	498.795	311.051	358.06	256.298	290.488	266.276	337.421	488.919	373.627	648.356	353.703
position3 $x_3$	498.882	310.558	358.084	256.363	290.354	266.194	337.497	488.916	374.015	648.385	353.453
position4 $x_4$	498.976	310.767	358.076	256.243	290.552	266.239	337.397	488.923	373.84	648.326	354.053
position5 $x_5$	498.837	310.8	357.711	256.382	290.421	266.338	337.529	488.697	373.993	648.279	353.701
position6 $x_6$	498.921	310.632	358.016	256.259	290.355	266.403	337.321	488.936	374.0	648.370	353.504
position7 $x_7$	498.942	310.594	357.991	256.359	290.306	266.336	337.283	488.743	374.24	648.428	353.458
position8 $x_8$	498.856	310.638	357.678	256.309	290.225	266.278	337.539	488.949	373.98	648.433	353.57
position9 $x_9$	498.887	310.69	357.977	256.458	290.417	266.265	337.386	488.864	374.079	648.287	353.769
position10 $x_{10}$	498.901	310.731	357.955	256.384	290.371	266.041	337.360	488.796	373.944	648.252	353.914
Exact value $x_E$	498.857	310.803	357.857	256.331	290.379	266.217	337.400	488.831	373.912	648.388	353.772
Average value $\mu$	498.890	310.749	357.930	256.362	290.371	266.278	337.413	488.876	373.993	648.366	353.670
Max error $E_{\max}$	0.119	0.248	0.227	0.234	0.173	0.191	0.139	0.188	0.328	0.136	0.319
Min error $E_{\min}$	0.001	0.003	0.098	0.022	0.006	0.022	0.003	0.033	0.032	0.005	0.003

## 6 Conclusions

(1) A photometric linearization method to eliminate the specular light on the tube's surface, and the diffuse reflection light component is proposed. The proposed method is effective in improving the quality of the tube image, which is the basis for accurate measurements of the tube endpoints.

(2) The linear segment length of the tube's end can be optimized using a least-squares method, allowing calculation of the spatial coordinates and the relative distance of the endpoints. This method does not require any surface treatment of the tube or any tools for the measurement.

(3) The calculation speed of the method is fast, and the operation is simple and can be mastered easily by inexperienced workers.

(4) The measurement method described can effectively meet the accuracy requirement of tube endpoint measurements in engineering.

## References

- [1] ZHOU C, YIN Y H. Pipe assembly planning algorithm by imitating human imaginal thinking[J]. *Assembly Automation*, 2010, 30(1): 66–74.
- [2] LI H, YANG H, SONG F, et al. Springback characterization and behaviors of high-strength Ti-3Al-2.5 V tube in cold rotary draw bending[J]. *Journal of Materials Processing Technology*, 2012, 212(9): 1973–1987.
- [3] KAWASHIMA K, KANAI S, DATE H. As-built modeling of piping system from terrestrial laser-scanned point clouds using normal-based region growing[J]. *Journal of Computational Design and Engineering*, 2014, 1(1): 13–26.
- [4] SON H, BOSCH F, KIM C. As-built data acquisition and its use in production monitoring and automated layout of civil infrastructure: A survey[J]. *Advanced Engineering Informatics*, 2015, 29(2): 172–183.
- [5] JAHANSHAH M R, MASRI S F. Adaptive vision-based crack detection using 3D scene reconstruction for condition assessment of structures[J]. *Automation in Construction*, 2012, 22: 567–576.
- [6] HEIST S, MANN A, KUHMSTEDT P, et al. Array projection of aperiodic sinusoidal fringes for high-speed three-dimensional shape measurement[J]. *Optical Engineering*, 2014, 53(11): 112208-1–112208-12.
- [7] HUANG J, LAN X, KAUR A, et al. Reflection-based phase-shifted long period fiber grating for simultaneous measurement of temperature and refractive index[J]. *Optical Engineering*, 2013, 52(1): 014404-1–014404-4.
- [8] WADE P, MORAN D, GRAHAM J, et al. Robust and accurate 3D measurement of formed tube using trinocular stereo vision[C]// *The British Machine Vision Conference*, Essex, UK, September 8–11, 1997: 1–10.
- [9] BERGAMASCO F, COSMO L, ALBARELLI A, et al. A robust multi-camera 3D ellipse fitting for contactless measurements[C]// *2012 Second International Conference on 3D Imaging, Modeling, Processing, Visualization and Transmission*, Zurich, Switzerland, October 13–15, 2012: 168–175.
- [10] OUELLET J N, HEBERT P. Precise ellipse estimation without contour point extraction[J]. *Machine Vision and Applications*, 2009, 21(1): 59–67.
- [11] USABIAGA J, EROL A, BEBIS G, et al. Global hand pose

- estimation by multiple camera ellipse tracking[J]. *Machine Vision and Applications*, 2009, 21(1): 1–15.
- [12] AHN S J, WARNECKE H, KOTOWSKI R. Systematic geometric image measurement errors of circular object targets: Mathematical formulation and correction[J]. *The Photogrammetric Record*, 1999, 16(93): 485–502.
- [13] JIN P, LIU J H, LIU S L, et al. Measuring method of pipeline endpoints based on two-dimensional point-target[J]. *Computer Integrated Manufacturing Systems*, 2014, 20(11): 2758–2766. (in Chinese)
- [14] SHAFER S A. Using color to separate reflection components[J]. *Color Research & Application*, 1985, 10(4): 210–218.
- [15] WOLFF L B, BOULT T E. Constraining object features using a polarization reflectance model[J]. *IEEE Transactions on Pattern Analysis & Machine Intelligence*, 1991, 13(7): 635–657.
- [16] UMEYAMA S, GODIN G. Separation of diffuse and specular components of surface reflection by use of polarization and statistical analysis of images[J]. *IEEE Transactions on Pattern Analysis and Machine Intelligence*, 2004, 26(5): 639–647.
- [17] SATO Y, IKEUCHI K. Temporal-color space analysis of reflection[J]. *Journal of the Optical Society of America A*, 1994, 11(11): 2990–3002.
- [18] KLINKER G J, SHAFER S A, KANADE T. The measurement of highlights in color images[J]. *International Journal of Computer Vision*, 1988, 2(1): 7–32.
- [19] NOVAK C L, SHAFER S A. Anatomy of a color histogram [C]// *1992 IEEE Computer Society Conference on Computer Vision and Pattern Recognition*, Illinois, USA, June 15–18, 1992: 599–605.
- [20] CHING W S, TOH P S, ER M H. A new specular highlights detection algorithm using multiple views [C]// *1993 International Conference on Information Engineering 93 Communications and Networks for the Year 2000*, Singapore, September 6–11, 1993: 474–478.
- [21] WANG C Q, ZHU F W. Removing highly illuminated regions from a single image[J]. *Journal of Shanghai university(Natural Science Edition)*, 2007, 13(2): 151–154. (in Chinese)
- [22] JIANG Y X, WANG X T, XU X G, et al. A method for image enhancement based on light compensation[J]. *Acta Electronica Sinica*, 2009, 37(4A): 151–155. (in Chinese)
- [23] BOSEMANN W. The optical tube measurement system OLM photogrammetric methods used for industrial automation and process control[J]. *International Archives of Photogrammetry and Remote Sensing*, 1996, 31(B5): 55–58.
- [24] NAYAR S K, IKEUCHI K, KANADE T. Surface reflection: physical and geometrical perspectives[J]. *IEEE Transactions on Pattern Analysis & Machine Intelligence*, 1991, 13(7): 611–634.
- [25] SHASHUA A. *Geometry and photometry in 3D visual recognition*[D]. Boston: Massachusetts Institute of Technology, 1992.
- [26] MUKAIGAWA Y, MIYAKI H, MIHASHI S, et al. Photometric image-based rendering for image generation in arbitrary illumination[C]// *Proceedings of Eighth IEEE International Conference on Computer Vision*, Vancouver, Canada, July 7–14, 2001: 652–659
- [27] FURUKAWA Y, PONCE J. Accurate camera calibration from multi-view stereo and bundle adjustment[C]// *Proceedings of IEEE Conference on the Computer Vision and Pattern Recognition*, Anchorage, USA, June 23–28, 2008: 1–8..

### Biographical notes

LU Shaoli, born in 1984, is currently a lecturer at *Beijing Institute of Technology, China*. She received her PhD degree from *Tsinghua University, China*, in 2012. Her main research interests include machine vision, on-line measurement, virtual assembly and image processing.  
Tel: +86-10-68912503; E-mail: liushaoli@bit.edu.cn.

JIN Peng, born in 1987, is currently a PhD candidate at *Beijing Institute of Technology, China*. He received his master degree from *North China Electricity Power University, China*, in 2013. His research interests include machine vision and photogrammetry.  
E-mail: kingpeng604@163.com

LIU Jianhua, born in 1977, is a professor, PhD advisor, and received his PhD degree in mechanical engineering from *Beijing Institute of Technology, China*. His scholastic interests include virtual assembly and machine vision. Now he has published over 60 research papers in virtual assembly.  
Tel: +86-10-68912503; E-mail: jeffliu@bit.edu.cn.

WANG Xiao, born in 1989, is currently a PhD candidate at *Beijing Institute of Technology, China*. He received his bachelor degree from *Beijing University of Chemical Technology, China*, in 2014. His research interests include machine vision and photogrammetry.  
E-mail: hnwangxiao@sina.com

SUN Peng, born in 1990, received his master degree from *Beijing Institute of Technology, China*, in 2015. His research interests include machine vision and photogrammetry.  
E-mail: sunpengfrank@sina.com